# Origin of high interfacial resistance in solid-state batteries: LLTO/LCO half-cells

Pengyu Xu[a], Wolfgang Rheinheimer[a][c], Avanish Mishra[b], Shoumya Nandy Shuvo[a], Zhimin Qi[a], Haiyan Wang[a], Avinash M. Dongare[b], Lia A. Stanciu[a]*

[a] Pengyu Xu, Shoumya Nandy Shuvo, Dr. Zhimin Qi, Dr. Wolfgang Rheinheimer, Dr. Haiyan Wang, Dr. Lia A. Stanciu

School of Materials Engineering, Purdue University, West Lafayette, USA

[b] Dr. Avanish Mishra, Dr. Avinash M. Dongare

Department of Materials and Engineering, University of Connecticut, USA

[c] Dr. Wolfgang Rheinheimer

Institute of Energy and Climate Research: Materials Synthesis and Processing (IEK-1), Forschungszentrum Jülich, Jülich, Germany

* Dr. Lia A.Stanciu

School of Materials Engineering; Birck Nanotechnology Center, Purdue University, West Lafayette, USA

## Abstract

The interface between cathode and electrolyte is a significant source of large interfacial resistance in solid state batteries (SSBs). Spark plasma sintering (SPS) allows densifying electrolyte and electrodes in one step, which can improve the interfacial contact in SSBs and significantly shorten the processing time. In this work, we proposed a two-step joining process to prepare cathode ($LiCoO_2$, LCO) / electrolyte ($Li_{0.33}La_{0.57}TiO_3$, LLTO) half cells via SPS. Interdiffusion between $Ti^{4+}/Co^{3+}$ was observed at the interface by SEM/STEM. Resulting in the formation of Li-Ti-La-Co-O phase, Li-Ti-Co-O phase in LLTO and Li-Co-Ti-O phase in LCO. Computational modeling has been used to verify that the Li-Ti-Co-O phase has a $LiTi_2O_4$ host lattice. In a study of interfacial electrical properties, the resistance of this interdiffusion layer was found to be $10^5$ Ω, which is 40 times higher than the resistance of the individual LLTO phase. The formation of an interdiffusion layer is identified as the origin of high interface resistance in LLTO/LCO half-cell.

## Table of contents:

LLTO/LCO half-cells were prepared by a 2-step joining process. Electron Microscopic analysis have been applied to the interfacial region. We identified 3 additional regions formed by interdiffusion between Ti/Mn. The resistance of such interdiffusion layer is $10^5\Omega$ and is considered as the main origin of interfacial resistance in LLTO/LCO half-cell.

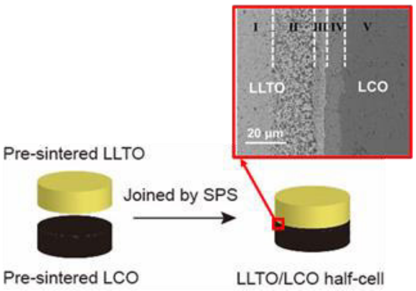

**Keywords: LLTO, half-cell, interphase, interdiffusion.**

## 1. Introduction

All-solid-state lithium ion batteries have been recognized as promising candidates for next generation energy storage devices.[1] In solid state batteries (SSBs), traditional liquid electrolytes are replaced by nonflammable solid electrolytes. Therefore, SSBs are expected to have outstanding safety performance[2]. Moreover, ceramic solid electrolytes typically provide broad electrochemical windows (>5V)[3] and high mechanical strength[4]. Thus, SSBs would have larger energy densities and longer cycling life[5–7].

At the same time, there are some challenges hindering the commercialization of SSBs. The poor ionic conductivity of solid electrolytes (SEs) as well as the high interfacial resistance between SEs and electrodes are the two primary obstacles confronting SSBs[8]. Large internal resistance in SSBs could lead to considerable ohmic loss, low power density and poor cycling performance [9]. Over the past decades, significant improvements have been achieved in elevating the ionic conductivities of SEs[10]. $Li_2S$-$P_2S_5$[11] and $Li_{10}GeP_2S_{12}$[12] electrolytes were reported to have ionic conductivities above $10^{-2}$ S/cm, which is comparable with traditional liquid electrolytes. Other oxide solid electrolytes such as $Li_{0.33}La_{0.57}TiO_3$ (LLTO)[13], $Li_{1.3}Al_{0.3}Ti_{1.7}(PO_4)_3$ (LATP)[14] and $Li_{6.4}La_3Zr_{1.4}Ta_{0.6}O_{12}$ (Ta-doped LLZO)[15] exhibit ionic conductivities in the order of $10^{-3}$ S/cm.

Despite the progress in SEs, our understanding of interfacial phenomena is still lagging, few studies have been reported on this topic[16–23] for solid state lithium ion batteries. Engineering the properties of the cathode/electrolyte interface is highly dependent on our ability to understand ion transport mechanisms for candidate solid electrolytes and cathode materials, which is the focus of this study. The formation of interfacial phases (interphases)[18,24], space-charge layer effects[19,20] and poor contact between electrodes and electrolyte[21] are the most important sources of interfacial resistance. Interphases formed by interdiffusion between cathode and electrolyte materials have been widely observed in SSBs, resulting in large interfacial resistances. The Meng group[22] reported an interphase at the $LiCoO_2$/ LiPON interface using scanning transmission electron microscopy (STEM). The interphase was argued to cause irreversible capacity loss in the battery. Sakuda[23] investigated $LiCoO_2$/$Li_2S$-$P_2S_5$ interfaces after charging. Again, a clear interfacial layer was detected by STEM and energy dispersive spectroscopy (EDS). The Ceder group[25] theoretically testified the formation of interphases in multiple cathode/electrolyte combinations. Therefore, understanding the formation mechanism of this interphase and investigating its impact on battery resistance could be critical in engineering a structurally stable SSB.

On the experimental side, conventional co-sintering of cathode and electrolyte materials could provide sufficient interfacial contact for lowering the interfacial resistance of the half-cell[26,27]. Compared with the other interfacial modification techniques such as buffer layer deposition[28,29], interface softening[30] and surface coating[31], co-sintering is the most convenient and economical method. However, the high temperature during co-sintering can lead to severe interdiffusion and cause undesired chemical reactions between cathode and electrolyte materials[32,33]. Spark plasma sintering (SPS) offers many benefits over conventional sintering; by applying uniaxial pressure and large pulsed DC current to the sample, SPS consolidates powders in a much shorter sintering time and at relatively lower temperature[34]. As a result, the formation of interphases could be alleviated in the SPS process, which makes SPS a promising technique in manufacturing cathode/electrolyte/anode SSB cells[35]. An additional new insight this work is putting forward stems from the fact that the electric field effects in SPS on the interdiffusion process, which could potentially lead to the formation of metastable phases, is still not fully understood[36,37]. This potential effect is addressed here via parallel hot-pressing experiments of the cathode/electrolyte material pairs, followed by characterization.

It is now clear that to produce effective SSBs for industrial applications, an interphase with minimized ionic conduction resistance is desired. Thus, this work focuses on understanding the mechanisms of the interphase formation and its influence on ionic conductivity, which in turn could shed light on the appropriate choices of cathode/electrolyte materials. Lithium Lanthanum Titanite ($Li_{0.33}La_{0.57}TiO_3$, LLTO) is a well-known perovskite electrolyte with high bulk conductivity. LLTO is a very strong competitor among SEs when considering large-scale manufacturing SSBs.[38] LLTO is easy to handle and it is very stable in air against high moisture environment[39]. Moreover, LLTO displays high electrochemical stability(>8V)[40] as well as good thermal stability in the temperature interval 4K-1600K[41,42], which make LLTO a perfect candidate for investigations of interfaces in co-sintered cathode/electrolyte half-cells. In previous study[43], we investigated the interfacial phenomena in $Li_2MnO_4$(LMO)/$Li_{0.33}La_{0.57}TiO_3$(LLTO) half cells. The impedance of the half-cell was dominated by the interphase. In this work, we selected $LiCoO_2$ (LCO) as cathode material and investigated the feasibility of applying LLTO/LCO half-cell pair to an SSB. $LiCoO_2$ (LCO) is a cathode material currently in use for commercial batteries and offers a balance between capacity and cycling stability[44,45]. For the first time, we co-sintered the LCO and LLTO with a two-step joining process via SPS to investigate the interphase formation in this system. Scanning Electron Microscopy (SEM), Scanning Transmission Electron Microscopy (STEM), High Resolution Transmission Electron Microscopy (HRTEM), Energy Dispersive X-ray Spectroscopy (EDS) and Electron Energy Loss Spectroscopy (EELS) were applied to characterize the LCO/LLTO interface. The influence of the interphase formation on the resistance of LCO/LLTO half-cell pair was analyzed by Electrochemical Impedance Spectroscopy (EIS) and computational modelling.

## 2. Experimental Procedure

### Powder synthesis

$Li_{0.33}La_{0.57}TiO_3$ (LLTO) powders were prepared by the mixed-oxide/carbonate route[43]. $Li_2CO_3$ (Sigma-Aldrich, ≥99%), $La_2O_3$(Sigma-Aldrich, ≥99%) and $TiO_2$ (Rutile, Sigma-Aldrich, ≥99%) were mixed stoichiometric ally in ethanol with an attrition mill. The mixed powders were dried and calcined in a tube furnace at 1050°C for 6 hours in air to form the perovskite phase. Next, the LLTO powders were attrition-milled again for 2 hours to break agglomerates formed during calcination. Finally, the powders were sieved (100µm, Gilson company). The cathode material $LiCoO_2$ was commercially available from Sigma Aldrich (442704, purity of 99.8%).

### SPS Co-sintering

Mixed LCO and LLTO powders were co-sintered by SPS to produce an LLTO/LCO mixture pellet. This pellet is analyzed to understand any chemical reactions that may occur[46]. LCO and LLTO powders were mixed at a volume ratio of 1:1 in a mortar. The thoroughly mixed powders were sintered by SPS at 850°C and 50 MPa for 10 minutes, with a heating and cooling rate of 100°C/min.

LLTO/LCO half-cells joined via SPS were prepared through a two-step joining process[47,48] as sketched in Figure 1(a). In the first step, LLTO and LCO powders were first sintered individually by a Thermal Technology SPS 10-3 machine into 1mm thick pellets. The pellets were sintered at 850°C and 50MPa for 10 minutes, with a heating/cooling rate of 100°C/min. To relief the thermal stress at the interface and avoid the formation of cracks, a separate joining process was designed at a lower temperature of 700°C [48]. LLTO and LCO pellets were polished with SiC paper (800 Grit) and then joined by SPS at 700°C and 20MPa for 10 minutes. The heating rate was 100°C/min and the cooling rate was 10°C/min. Subsequently, the joined pellet was cut with a diamond blade and embedded in epoxy. The cross-section was polished by SiC paper and diamond slurry down to 1µm particle size.

LLTO/LCO half-cells joined via hot-pressing are prepared by a similar procedure, in an attempt to understand whether the electrical field had any effect on interfacial structure and composition. Thus, LLTO and LCO were pre-sintered by SPS respectively at 850°C and 50MPa for 10 minutes. The pellets were polished with SiC paper (800 Grit) and then joined in vacuum by a Centorr, Testorr$^{TM}$ series hot pressing machine to identify the possible impact of electric fields during the bonding process. The joining process was carried out at 700°C, 20MPa for 2 hours, with a heating rate of 25°C/min to 675°C, 5°C/min to 700°C and a cooling rate of 10°C/min.

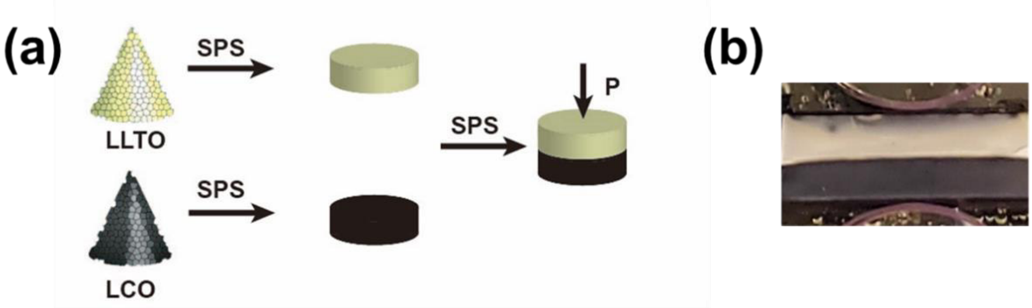

**Figure 1.** (a) Procedure of the two-step joining experiment for LCO/LLTO half-cells joined via SPS. (b) Polished cross-section of LCO/LLTO half-cell joined via SPS.

### Materials Characterization

XRD (Bruker D8 Focus, 2θ from 15° to 80°) and SEM-EDS (FEI Quanta 3D and Oxford Instruments) was used to characterize powders and samples.

For the LCO/LLTO half-cell in Figure 1(b), microstructures and elemental composition of the interfacial region were investigated by SEM, EDS line scans and EDS mappings. For TEM characterization, 10μm-20μm long lamellas were cut and lifted-out from the interfacial region by a Focused Ion Beam microscope (FIB, FEI Quanta 3D). Lamellas were thinned to 100nm thickness for HRTEM, STEM, EDS and EELS characterization. HRTEM, STEM and EDS were carried out by a FEI Talos 200X TEM, STEM/EELS characterization were made by a Themis Z TEM, the dispersion is 0.05 eV/ch, while the energy resolution is 1.1eV.

Electrochemical impedance spectroscopy (EIS) was also applied to SPS sintered LLTO, LCO and the joined LCO/LLTO pellets to determine the effect of the interphase on the overall resistance. EIS measurement was carried out by a BioLogic electrochemistry potentiostat from 1 Hz to 1MHz.

## 3. Results and Discussion

### Powder characterization and phase composition

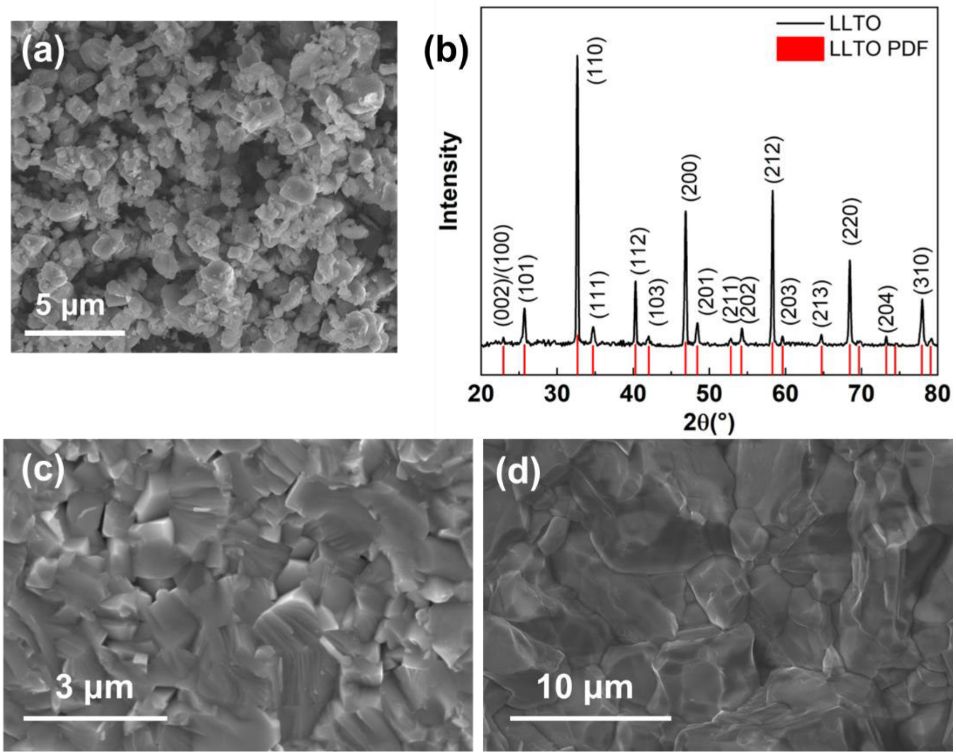

**Figure 2.** (a) SEM image of synthesized LLTO powders. (b) XRD pattern of the LLTO powders. The indexing relies on the standard PDF card JCPDS No.870935. (c) Inner morphology of SPS sintered LLTO pellet. (d) Inner morphology of SPS sintered LCO pellet

Microstructural and compositional characterization of powder precursors has an impact on the understanding of the properties of the sintered samples after processing. Figure 2 (a) and (b) show SEM and XRD characterization of LLTO powders. Based on Figure 2 (a), the particle size for LLTO powders is about 1µm. Figure 2 (b) shows the XRD pattern of LLTO powders. According to the standard PDF card JCPDS No.870935, the synthesized LLTO is phase-pure perovskite $Li_{0.33}La_{0.57}TiO_3$. The inner morphologies of SPS sintered LLTO and LCO as showed in Figure 2(c) and (d). Both pellets reach relative density of >95% according to Archimedes' method.

XRD, SEM and EDS have been applied to analyze possible reactions between LLTO and LCO powders after co-firing a powder mixture. Figure 3(a) shows the XRD pattern of SPS sintered LCO/LLTO powder mixture. According to the standard PDF cards, we identified two extra peaks (marked with stars) that match $Li_{1.47}Co_3O_4$ indicating a minor phase transformation during co-sintering. The corresponding microstructure and SEM-EDS mappings are presented in Figure 3(b). In the SEM image, based on Z contrast, we identified the darker phase as LCO and the brighter phase as LLTO. According to the SEM-EDS mappings in Figure 3(b), it is likely that some interdiffusion between $Ti^{4+}$ and $Co^{3+}$ occurred. However, very little $La^{3+}$ interdiffusion is visible. These results indicate that LLTO and LCO would not have significant chemical reaction at bulk phase scale. Still, the interdiffusion process could potentially result in an interphase formation with a thin layer of other phases below the detection limit of XRD and SEM-EDS[43].

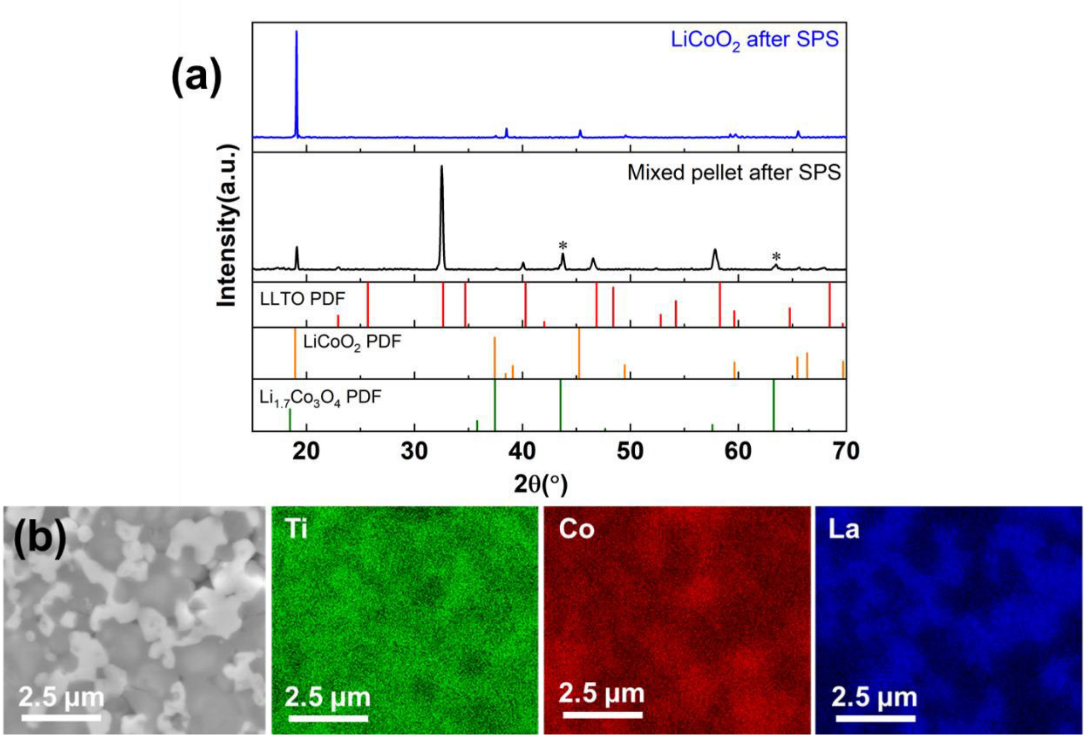

**Figure 3.** (a) XRD pattern of SPS densified LLTO/LCO mixture pellet. The pattern was compared with standard PDF card of LCO (JCPDS No.500653) and LLTO. The extra peaks (marked with stars) match with $Li_{1.47}Co_3O_4$ (JCPDS No.782040). (b) SEM image and element mapping for the powder mixture pellet after SPS

## Electron microscopy characterization of LCO/LLTO half-cell

The LCO/LLTO half-cell was prepared by a SPS joining method as sketched in Figure 1 (b). SEM and EDS were used to investigate the microstructure and chemical composition of the interface. Based on the contrast in Figure 4(a), the interface contains five different layers. As LLTO contains heavier elements than LCO, it results in brighter contrast in BSE-SEM (region I). Region II is more than 20µm thick and contains a two-phase microstructure with bright grains (phase α) and dark grains (phase β) intercalating each other. From the microstructural appearance, region II might be the result of a phase decomposition of a single-phase during cooling. Note that in Figure 4(d), this layer seems to be porous. This is due to breakout during polishing. Region III is another 5µm thick layer, the microstructure of which is similar to Region II but the dark grains are not present in this region. Region IV is a few microns thick layer, with slightly brighter contrast compared to LCO in region V.

Based on the SEM-EDS mapping in Figure 4(b) and EDS analysis in Figure S1 and Figure S2 (supplementary information), interdiffusion between $Co^{3+}$ and $Ti^{4+}$ is evident while limited $La^{3+}$ diffusion into the LCO is observed. This result agrees with Figure 3(b). However, a higher resolution characterization method is necessary for the interdiffusion analysis, particularly to resolve the composition of the two phases in region II. High resolution characterization methods, such as STEM/ EDS, STEM/EELS and HRTEM have been applied to these interfacial regions (region II, region III and region IV).

In general, the interdiffusion documented in Figure 4 is similar to other half-cell combinations. LMO-LLTO half-cells form a very similar interfacial structure with similar interdiffusion layer width[43]. Kim[24] applied EDS line scans to detect the interdiffusion between LCO and LLZO and confirmed the presence of an interphase as well.

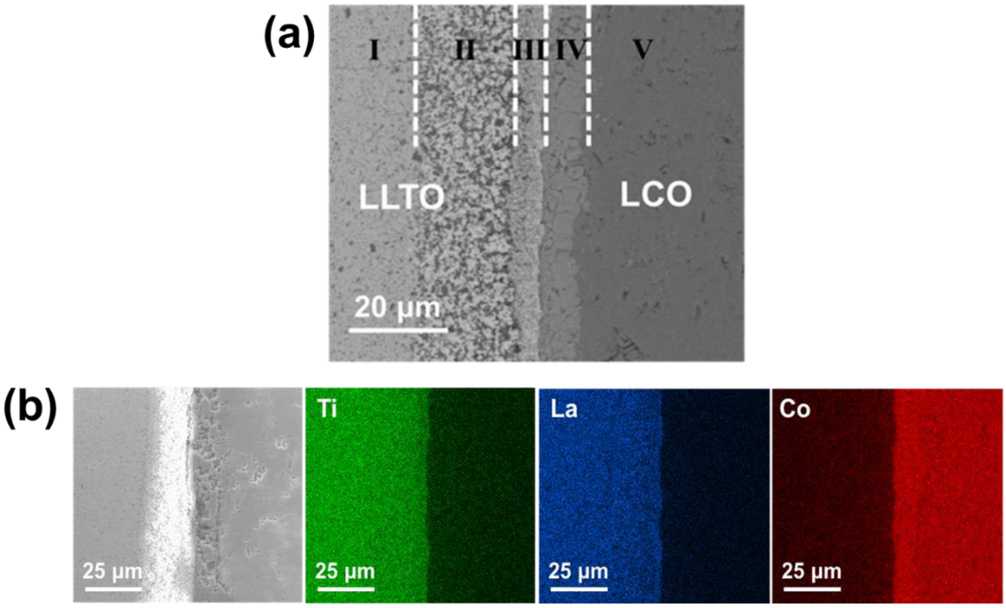

**Figure 4**. (a) Backscattered SEM image of LLTO/LCO interface, LLTO is the brighter phase (left) and LCO is the darker phase (right). The interfacial area contains five regions with different microstructures. I is LLTO phase, II is an intercalation region, III is a layer similar to II but without the second phase, IV is an LCO phase with contrast against V, V is LCO. (b) SEM image and element distribution profiles obtained by EDS mapping.

Figure 5(a) shows a 20µm long FIB sample containing region II, region III, region IV and a small part of region V in Figure 4(a). STEM/EDS characterization is applied to the entire sample area. From the HAADF-STEM image in Figure 5(b), four areas are identified for further chemical quantification (Table 1). Area 1 and Area 2 are from region II (Figure 4) containing bright (phase α) and dark grains (phase β) intercalated with each other. Area 1 is closer to the bulk LLTO and contains fewer dark grains than area 2. Area 3 lies within an interphase between LLTO and LCO, corresponding to region IV (Figure 4). Area 4 is from region phase V. From Figure 5(b) and Area 3 (table 1), we can conclude that the region IV (interphase) contains $Ti^{4+}$ and $Co^{3+}$ but no $La^{3+}$, which indicates the presence of $Co^{3+}$/$Ti^{4+}$interdiffusion at the interface. However, the JPDS database does not contain any Li-Co-Ti-O compound that matches the Co/Ti ratio of 1:1 so that the exact identity of this phase remains unclear. Given the location of this interphase in region IV (Figure 4(a)), we believe that this interphase has an LCO host lattice with some dissolved Ti.

The Co profiles indicate a rapid Co concentration decay from area 2 towards area 1. In area 4, the EDS results show no existence for any $Ti^{4+}$ or $La^{3+}$. Therefore, the STEM/EDS results are in disagreement with the hundreds of microns diffusion as detected by

SEM. As discussed above, the TEM/EDS results seem to be more reliable because of less secondary X-ray emission compared to SEM. Moreover, Figure 5(b) indicates that $Co^{3+}$ has a much longer diffusion distance compared with $Ti^{4+}$. Based on this data, we can conclude that $Co^{3+}$ has a higher diffusion rate than $Ti^{4+}$.

To further investigate the chemical composition of bright and dark grains in area 2, high-resolution STEM/EDS scans were carried out as showed in Figure 5(c) and (d). The Li concentration was investigated by EELS analysis as showed in Figure 5(e) and (f). Based on EDS mappings (Figure 5(b) - (d)) and area scans (Area 5, Area 6 in Table 1), we conclude that in region II, the $La^{3+}$ concentration in phase β is negligible. Chemical analysis of Area 5 and 6 (Table 1) reveals that the Ti/La ratio in phase α is lower than the 1/0.57 expected for LLTO. This indicates that $La^{3+}$ diffused from phase β to α. Moreover, phase α also has less $Ti^{4+}$ than phase β.

Based on Figure 5(c), the cobalt concentration in phase α is smaller than in phase β. An accumulation of $Co^{3+}$ was observed at the interface between α and β in the cobalt mapping, possibly indicating a complexion[43], space charge or a kinetic accumulation during particle growth (Figure 5(c), Figure 5(d)).

Additionally, to verify lithium presence in the phase α and β in region II, an EELS line scan was carried out in Figure 5(c). Spectrums from 4 points (marked in Figure 5(c)) are showed in Figure 5(e). La $N_{4,5}$ Peaks were only observed in the bright grain spectrums (B1,B2), while the peak position is most likely shifted due to the oxidation state of La[49]. This observation accords well with the TEM-EDS results. Li K-edges were observed in phase α at about 62eV, while one measurement of the phase β (D2) showed a Li K-edge at about 58eV. In D1, there is also a Li K-edge present just below 55eV. This peak shift of the Li K-edge indicates a change in the chemical environment for lithium[50,51]. Additionally, the lithium concentration mapping in Figure 6(f) shows a much higher lithium concentration in α compared to β. Thus, we draw the conclusion that phase α contains Li, Ti, La, O with minor Co concentration. Phase β contains Li, Ti and O with a higher Co concentration compared with phase α.

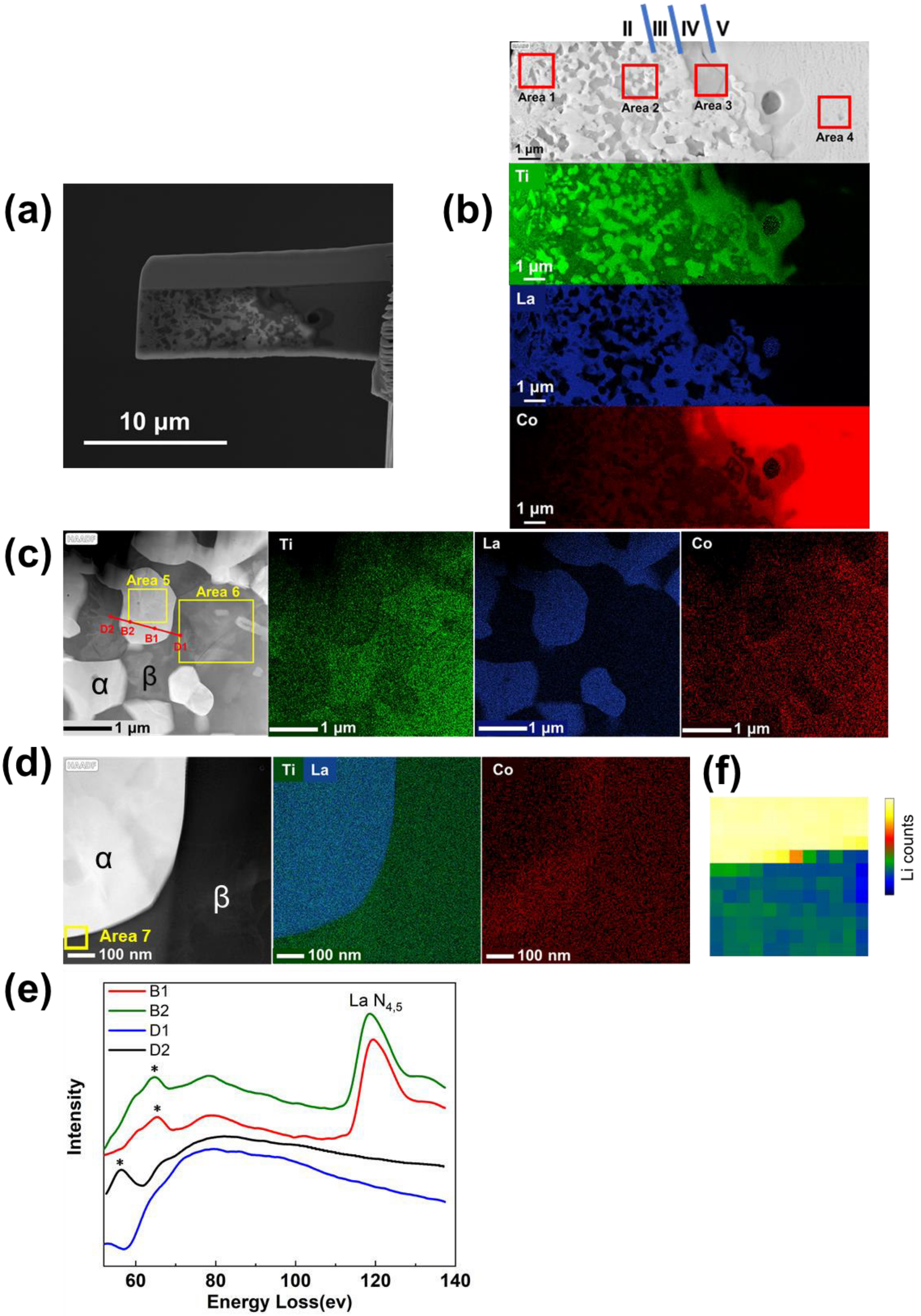

**Figure 5.** (a) SEM image of the lamella lift-out from the interfacial region. (b) Chemical mappings of the entire lamella as obtained by STEM/EDS. The four marked areas were analyzed in detail. II, III, IV, V refer to the same regions in Figure 4(a). (c) Chemical mapping of area 2 from (b) as obtained by STEM mapping. Again, two areas are marked. (d) Element concentration mapping of phase α/β interface. (e) EELS analysis of four points (B1, B2, D1 and D2) in (c). Lithium related peaks were marked out by stars. (f) Li concentration mapping for the area marked in (d). The color codes for Li counts in arbitrary units. The chemical composition was quantified by TEM-EDS area scans as detailed in Table 1.

**Table 1** Chemical composition for the six areas marked in Figure 5(b) and (c), as obtained by STEM/EDS area scans.

| | Atomic Fraction (mol%) | | | | | |
|---|---|---|---|---|---|---|
| Element | Area 1 | Area 2 | Area 3 | Area 4 | Area 5 | Area 6 |
| O | 55.73 | 54.19 | 55.46 | 41.9 | 64.47 | 74.96 |
| Ti | 27.34 | 25.43 | 21.37 | 0.05 | 15.79 | 22.07 |
| Co | 1.76 | 7.88 | 23.17 | 58.04 | 0.28 | 2.7 |
| La | 15.17 | 12.5 | 0 | 0.01 | 19.46 | 0.26 |

To confirm the $Co^{3+}/Ti^{4+}$ interdiffusion would lead to the formation of interphase in the LLTO/LCO half-cell, it is necessary that we eliminate the electrical field effects from the SPS process. Therefore, a hot-pressing joining has been applied to the pre-sintered LLTO, LCO pellets. Similar to the previous discussed approach, a 15μm lamella was cut and lift-out from the interfacial region of the hot-pressing LLTO/LCO sample. HAADF STEM and EDS has been applied to identify phase composition information. From the HAADF STEM image in Figure 6(b), we noticed that the microstructure in this hot-pressing interface is very similar to that of SPS sample (Figure 5(b)), the interfacial region still an intercalation region (region II) and a new phase in LCO side (region IV). Additionally, the EDS mappings in Figure 6(b) confirmed that the phase composition in this hot-pressing sample is the same as previous discussed SPS sample. Thus, we can safely draw the conclusion that the interdiffusion process in LLTO/LCO half-cell is not affected by the electric field and current during SPS.

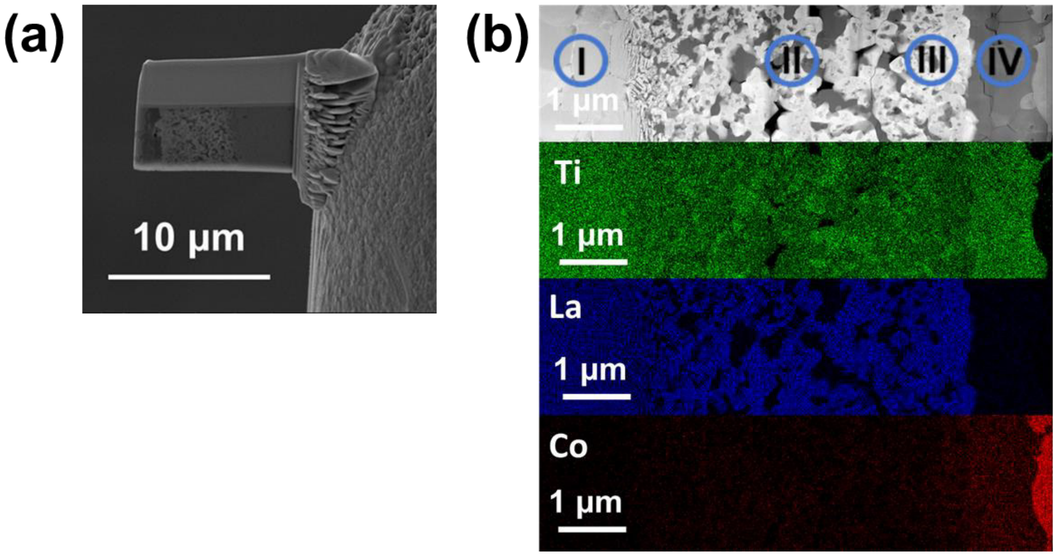

**Figure 6.** (a) SEM image of the lamella lift-out from the interfacial region of hot-pressing sample. (b) HAADF image and EDS mapping of the sample in (a).

To further investigate the interface between α and β in layer II for any interphase or complexion[52] in the intercalation region, HRTEM was applied to the interface in

Figure 5(d) as showed in Figure 7 (a), (b). Figure 7 (b) revealed a tilted grain boundary between phase α and β grains. Phase α is crystalline perovskite phase while phase β has a $LiTi_2O_4$ host lattice. This finding is underlined by SEAD patterns presented in Figure 7(c), (d) and Figure S3 in supplementary information. Based on Figure 7(c) and (d), we can determine that the crystal has an FCC lattice with lattice parameter of ~8.4 Å. After checking JCPDS database and matching with modeling result in Figure 8(b). The β phase diffraction pattern fits $LiTi_2O_4$ lattice (JCPDS No.400407). The Ti/O ratio from the EDS analysis of β phase (Area 6) deviates from 1:2, as the oxygen signal is very noisy due to artifacts induced by sample processing and preparation. Thus, the EDS results on oxygen fraction have only a guidance value rather than provide precise composition information. However, there is no evidence of a complexion other than the Co enrichment discussed with Figure 5(c) and (d).

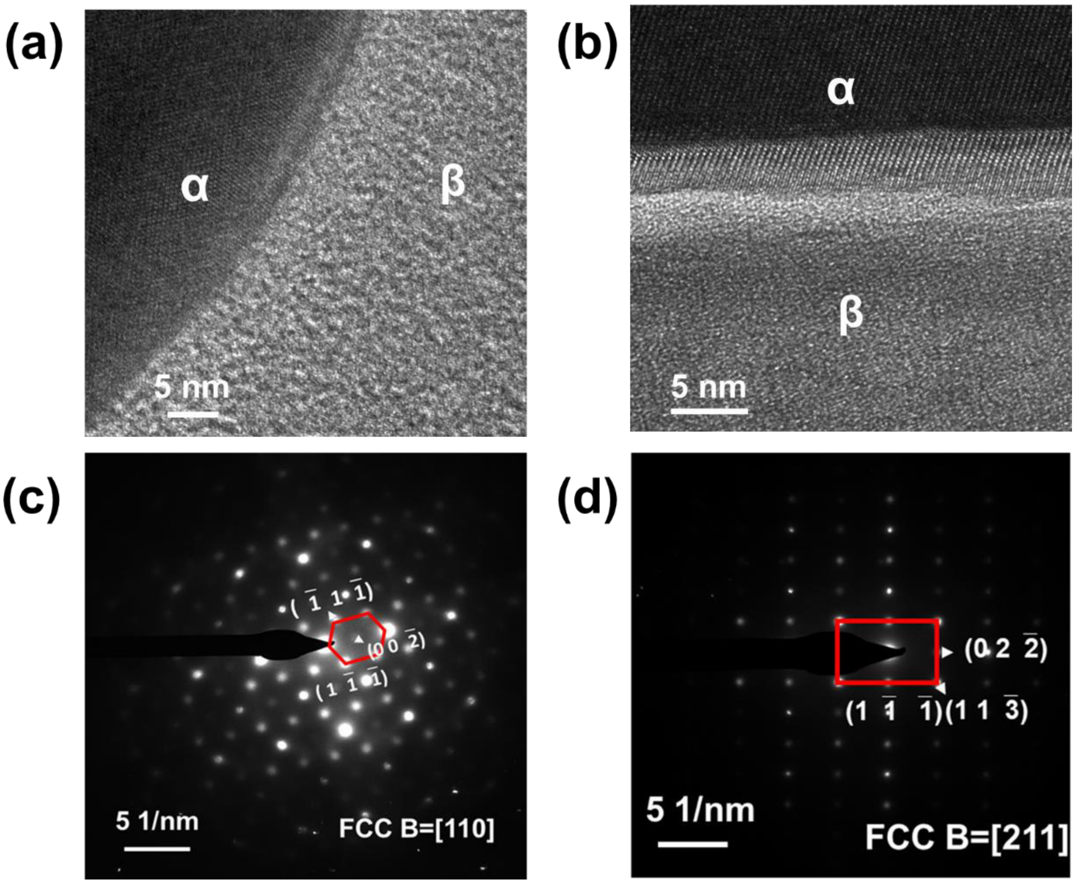

**Figure 7**. HRTEM image of bright (phase α) and dark grain (phase β) interface. (c) SEAD pattern of β grain in [110] zone, (d) SEAD pattern for β grain in [211] zone.

In summary, the analytical TEM reveals that at the interfacial region in LCO/LLTO half-cells, three additional layers (II, III, IV) have been identified by SEM/TEM observations. In Region II (Figure 4(a)), we identified two different phases (α, β) intercalating. Analytical TEM reveals that phase α is a crystalline Li-La-Ti-Co-O compound in perovskite phase, while the phase β is an Li-Ti-Co-O compound with a

$LiTi_2O4$ host lattice. Phase α is rich in Li while phase β has higher Co and Ti concentration. Region III is a thin layer of phase α (Li-La-Ti-Co-O). Region IV is another few micron thick layer with LCO host lattice containing some $Ti^{4+}$. However, none of these compounds could be identified as a separate phase based on stoichiometry and the JCPDS database.

The EDS analysis for the interphase in Region III clearly indicated that an interdiffusion between $Co^{3+}$ and $Ti^{4+}$ occurred. $Co^{3+}$ has a higher diffusion rate compared with $Ti^{4+}$. In the perovskite LLTO, $La^{3+}$ cations have a coordination number of 12 and $Ti^{4+}$ have a coordination number of 6. In the LCO phase, $Co^{3+}$ has a coordination number of 6. The ionic radii of these cations are 150 pm ($La^{3+}$), 74.5pm ($Ti^{4+}$) and 75pm ($Co^{3+}$)[53]. Diffusion of La ions into the LCO are limited by a large misfit in ionic radius. However, as the $Ti^{4+}/Co^{3+}$ couple have very similar ionic radii, like a substitutional interdiffusion process occurred. The diffusion distance for $Ti^{4+}$ was about 2μm in the interphase layer, while the $Co^{3+}$ diffusion distance was about 20μm. As more $Co^{3+}$ diffused in LLTO than $Ti^{4+}$ diffused in LCO, it is possible that some Co vacancies are introduced in LCO thereby changing the point defect chemistry.

## Computational Simulations of β Phase Composition

As observed in the experimental diffraction pattern of β phase (dark grains) showed in Figure 7(c) and (d), indicate the existence of FCC structure Li-Ti-O phase with a lattice parameter of ~8.4 Å. However, there could be various possible combinations of Li-Ti-O with different stoichiometry with FCC crystal structure and similar lattice parameter. To identify the possible stable compound with FCC crystal structure, we constructed a phase diagram of Li-Ti-O at 0K using the “phase diagram” package of the pymatgen library[54,55] . The solid dots/nodes in Figure 8 show stable compositions, whereas red and blue nodes highlight stable ternary phases. Other than $LiTi_2O_4$ (blue node), the rest compositions do not possess FCC symmetry (Fd-3m) for the minimum energy phase. The calculated lattice parameter for FCC $LiTi_2O_4$ is 8.46 Å, which is close to the observed value from the diffraction experiment. Besides, $LiTiO_2$ also exhibits an FCC crystal structure, but for a higher energy phase.

Further, to validate that the observed structure is $LiTi_2O_4$, we simulated the virtual selected area-electron diffraction (SAED) patterns for the FCC phase for comparison with the experimental findings. The SAED patterns are simulated for a supercell of $LiTi_2O_4$ using the Large-scale Atomic/Molecular Massively Parallel Simulator (LAMMPS) [56] user-diffraction package[57,58] . For SAED, an irradiation wavelength of 0.0251 Å (200-keV electron radiation) and a cutoff radius to 1.25 Å−1 are utilized. The SAED patterns are visualized for [110] and [211] zone axes to compare with experimental prediction. The SAED patterns are shown in Figure 8 (b) and show similar spots to those observed in the experimental diffraction patterns. The simulated SAED patterns confirm the formation of phase β with a $LiTi_2O_4$ structure and a lattice parameter of ~8.4 Å.

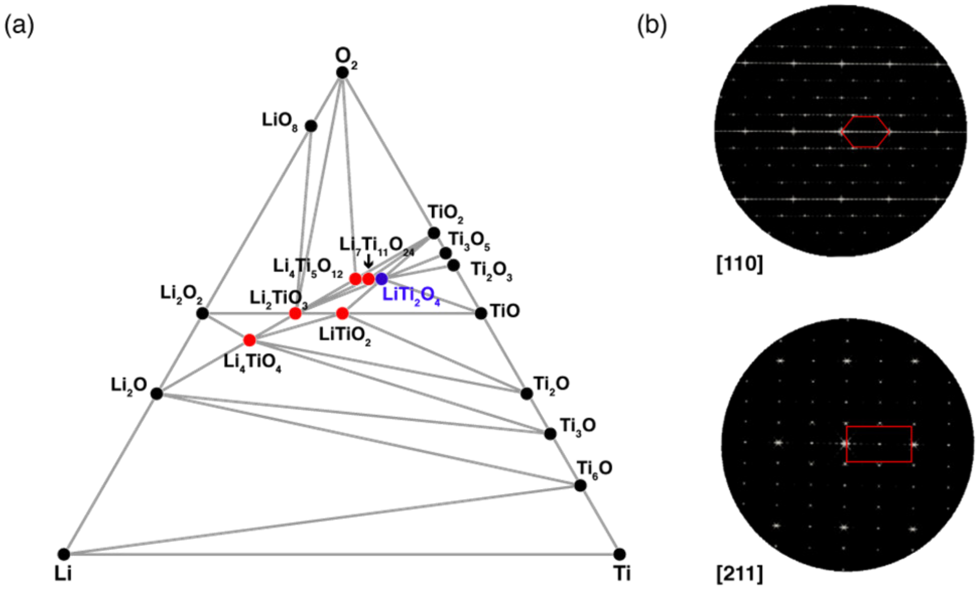

**Figure 8**. (a) Simulated phase diagram for Li-Ti-O to confirm possible structure with FCC symmetry. The red dots represent stable structure with combination Li-Ti-O, and the blue dot indicates stable structure with FCC as minimum energy phase ($LiT_2O_4$). (b) The simulated virtual selected area-electron diffraction (SAED) patterns of FCC $LiT_2O_4$ along [110] and [211] zone axes.

## Electrical Characterization of the LCO/LLTO half cell

It was showed before that the formation of an interphase by interdiffusion can lead to very large interfacial resistance[43], which is undesirable in SSBs. This interphase layer appears as an additional part in the Nyquist plot of electrochemical impedance spectroscopy (EIS)[18]. In the present study, EIS analysis was carried out for an LCO/LLTO half-cell joined by SPS (700°C, 10 minutes, 20MPa).

Figure 9(a) shows the impedance profile of an LLTO pellet sintered by SPS (850°C, 10 minutes, 50MPa). An equivalent circuit[43,59]as shown in Figure 9(a) was used to fit the impedance data. The fitting parameters are listed in Table S2 in the supplementary information. Based on the equivalent circuit applied in Figure 9(a), the grain boundary impedance is expected to contribute to the lower frequency part compared with grain resistance. Therefore, the grain boundary resistance for LLTO was 2714Ω yielding a grain boundary conductivity of $\sigma_{gb} = \rho\frac{l}{s} = 4.69\times10^{-5}\ \mathrm{S/cm}$. The bulk conductivity of LLTO including both grain and grain boundary resistance was found to be $4.62\times10^{-5}$ S/cm. This is comparable with the LLTO bulk conductivity reported in the literature[60].

The impedance profile of the LCO pellet sintered by SPS (850°C, 10 minutes, 50MPa) is showed in Figure 9(b). Both electronic and ionic conductivity occur in LCO[61,62]. Therefore, the equivalent circuit in Figure 9(b) was used. The fitting parameters are listed in Table S3 (supplementary information).

Figure 9(c) shows the impedance of the LCO/LLTO half-cell along with LCO and LLTO. The impedance of LLTO is two order of magnitude lower than that of LCO and

LCO/LLTO (see inset). The LCO/LLTO impedance is two times larger than the LCO impedance. Accordingly, the interfacial resistance is in the same order of magnitude as the LCO bulk impedance. To obtain detailed information on the impedance signal of the interphase, a subtraction method had been applied to analyze the data[43]. The imaginary part of the interphase ($Z_{\text{interphase}}$) was estimated based on the information of sperate LCO ($Z_{\text{LCO}}$) and LLTO ($Z_{\text{LLTO}}$):

$$\mathrm{Im}(Z_{\text{interphase}})=\mathrm{Im}(Z_{\text{LLTO/LCO}})-(\mathrm{Im}(Z_{\text{LLTO}})+\mathrm{Im}(Z_{\text{LCO}})). \qquad (1)$$

Analogue, the real part of interphase was estimated by:

$$\mathrm{Re}(Z_{\text{interphase}})=\mathrm{Re}(Z_{\text{LLTO/LCO}})-(\mathrm{Re}(Z_{\text{LLTO}})+\mathrm{Re}(Z_{\text{LCO}})). \qquad (2)$$

The calculated imaginary and real parts for this interphase were plotted in a Nyquist plot (-Im($Z_{\text{interphase}}$) vs Re($Z_{\text{interphase}}$)) showed in Figure 9(d), with a frequency range from 50kHz to 1Hz. In the Nyquist plot, we observed two semi-circles, which were fitted with two RC circuits. A single CPE element was also added to account for the low frequency tail. The corresponding equivalent circuit provides a reasonable fitting result in Figure 9(d). The fitting parameters are showed in Table S4 (supplementary information). Based on the fitting, it was evident that the interfacial resistance contains two parts. The total resistance for the interphase layer can be estimated based on R1(296730 Ω) and R2(160279 Ω), which adds to about $4.6\times10^{5}$ Ω.

Based on the equivalent circuit for the interphase we applied in Figure 9(d) and the equivalent circuits for separated LLTO and LCO, a circuit for the joined LCO/LLTO pellet can be obtained by placing the LLTO, LCO, interphase circuits in series. The circuit is showed in Figure 9(e). The grain impedance for LLTO is very low compared to the other components, therefore we neglected this part in the fitting process of the LLTO/LCO half-cell. The remaining parameters for LLTO and LCO were taken from the fitting in Figure 9(a) and (b) and were held constant. The parameters for the interphase (R5, CPE5, R6, CPE6) were obtained by fitting the LCO/LLTO impedance profile with the equivalent circuit in Figure 9(e). According to Figure 9(f) and Table 2, the fit is very accurate. From this data, the impedance parameters of the interphase are R5= 298010 Ω, Q5= $5.144\times10^{-11}$ F·s $^{a-1}$(a=0.99708), R6=108680 Ω and Q6=$1.7388\times10^{-8}$ F·s $^{a-1}$ (a=0.92347). These values agree well with the subtraction method in Figure 9(d). Therefore, we conclude that the interfacial resistance of LCO/LLTO contains two parts and the total resistance is about $4\times10^{5}$ Ω.

The effective capacity for a constant phase element can be calculated through the equation:

$$c_{\text{eff}}=Q^{1/a}R^{(1-a)/a} \quad (3)$$

Where Q and a are CPE parameters.

Using a plate capacitor approach, the obtained capacity can be used to calculate the thickness of the interphase layers, where:

$$d=\varepsilon_0\varepsilon_r A/C \quad (4).$$

$\varepsilon_0$ is the permittivity of vacuum and $\varepsilon_r$ is the relative permittivity. We approximate

$\varepsilon_r$=30 for LCO and LLTO. A is the cross-sectional area of the sample. The obtained thickness is 400µm for CPE5 and 2µm for CPE6. The 2µm layer matches the thickness of interdiffusion layer we observed in Fig. 5(b), while the layer thickness of 400µm probably stems from bulk LLTO or LCO. Therefore, resistance of the LLTO/LCO interdiffusion layer is $10^5$ Ω, which 40 times larger than the overall electrolyte resistance.

The EIS results underline that the interfacial resistance from the interdiffusion layer was still the major cause for the large internal resistance solid-state batteries and is likely to be a major problem to be overcome in such batteries[63]. Our group previously reported that this challenge does not only apply to LCO/LLTO half-cells, but also to LMO/LLTO half-cells[43]. Therefore, any cathode/electrolyte material pairs where an interphase is induced by interdiffusion is unfavorable for battery applications and needs to be suppressed carefully by choosing material combinations and processing methods that minimize this effect.

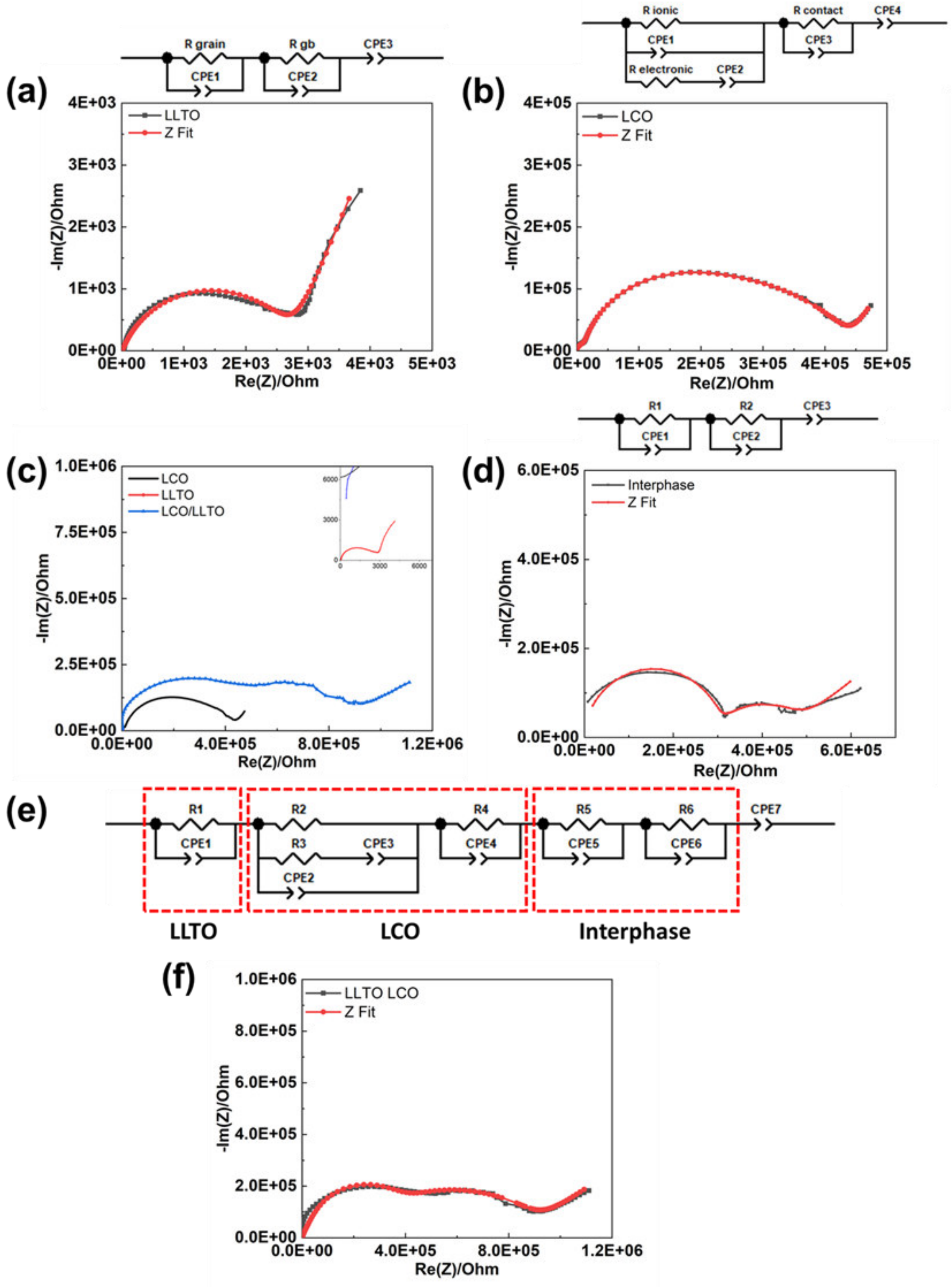

**Figure 9.** (a) Impedance profile of LLTO sintered by SPS. The equivalent circuit on the top was used for the fitting. (b) Impedance profile of LCO sintered by SPS along with the used equivalent circuit. (c) The impedance profiles of LLTO (red), LCO (black) and LLTO/LCO. (d) Nyquist plot of LCO/LLTO interphase from the subtraction method in the frequency range from 50kHz to 1Hz. (e) equivalent circuit for LLTO/LCO half-cell. (f) Impedance profile of LLTO sintered by SPS. The equivalent circuit from (e) was used for the fitting

**Table 2** Fitting parameters of LLTO/LCO impedance in Figure 9(f)

| Parameter | Value | Unit | Freedom |
|---|---|---|---|
| R1(LLTO) | 2714 | Ohm | Fixed |
| CPE1 (LLTO) | $1.218\times10^{-6}$ | $F\cdot s^{a-1}$ | Fixed |
| a1 | 0.766 | | Fixed |
| R2(LCO) | 429720 | Ohm | Fixed |
| CPE2(LCO) | $1.256\times10^{-6}$ | $F\cdot s^{a-1}$ | Fixed |
| a2 | 0.87965 | | Fixed |
| R3(LCO) | 672300 | Ohm | Fixed |
| CPE 3(LCO) | $8.807\times10^{-9}$ | $F\cdot s^{a-1}$ | Fixed |
| a3 | 0.66179 | | Fixed |
| R4(LCO) | 10262 | Ohm | Fixed |
| CPE4(LCO) | $1.254\times10^{-10}$ | $F\cdot s^{a-1}$ | Fixed |
| a4 | 1 | | Fixed |
| R5(interphase) | 298010 | Ohm | Free |
| CPE5(interphase) | $5.144\times10^{-11}$ | $F\cdot s^{a-1}$ | Free |
| a5 | 0.99708 | | Free |
| R6(interphase) | 108680 | Ohm | Free |
| CPE6(interphase) | $1.7388\times10^{-8}$ | $F\cdot s^{a-1}$ | Free |
| a6 | 0.92347 | | Free |
| CPE7 | $1.5643\times10^{-6}$ | $F\cdot s^{a-1}$ | Free |
| a7 | 0.40422 | | Free |

## Conclusions

In this work, we studied the interfacial properties between the commercial cathode material $LiCoO_2$(LCO) and the perovskite solid electrolyte $Li_{0.33}La_{0.57}TiO_3$(LLTO). A LCO/LLTO half-cell was prepared by a two-step joining process via Spark Plasma Sintering (SPS). The relatively low temperature of the joining process (700ºC) aims to relieve interfacial thermal stress and reduce temperature driven diffusion. Subsequently, interfacial microstructures and the effect of interphase formation on half-cell conductivity were investigated by analytical SEM, TEM and EIS. At the LCO/LLTO interface, we observed 3 layers in addition to the pure LLTO or LCO phases:

-Region II: Phases α and β intercalating with each other. Phase α is a crystalline Li-La-Ti-Co-O compound, with a LLTO host lattice. Phase β is a Li-Ti-Co-O compound, with a $LiTi_2O_4$ host lattice. Phase α is Li rich and phase β is Ti rich. This structure probably formed due to a phase decomposition during cooling.

-Region III: A few microns thick layer of phase α, no existence of phase β.

-Region IV: A few microns thick interphase layer of Li-Co-Ti-O compound, which is a LCO host lattice with some Ti content.

According to the EIS analysis, the formation of an interdiffusion layer contributes to an interfacial resistance of $10^5$ Ω, which is 40 times larger than that of the LLTO bulk phase. Therefore, we concluded that it is the interdiffusion between $Co^{3+}$ and $Ti^{4+}$ that results in great interfacial resistance in the LCO/LLTO half-cell pair, making this material selection unfavorable for SSB applications. To improve the performance of the SSBs it is mandatory that the interdiffusion of ions at the cathode/electrolyte interface is suppressed. Interphase engineering would be necessary to improve the ionic conduction. Cold-sintering[64] is a promising low temperature densification technique, which could be beneficial towards suppression of high temperature driven diffusion. Thus, this method has the potential of avoiding the formation of an interdiffusion layer, and therefore reduce the interfacial resistance. However, detailed studies will be needed in order to prove the feasibility of applying such technique to half-cell preparation.

### Corresponding Author

*Lia A Stanciu

E-mail: lstanciu@purdue.edu
Phone: +1 765 49-63552

School of Materials Engineering; Birck Nanotechnology Center, Purdue University, West Lafayette, USA

### Author Contributions

The manuscript was written through contributions of all authors. All authors have given approval to the final version of the manuscript. All of the authors were involved in the initial writing and final polishing phases.

### Notes

The authors declare no competing financial interest.

### Funding Sources

The project was financially supported by NSF under Award No. DMR 1734763.

### ACKNOWLEDGMENT

The authors would like to acknowledge financial support by NSF under Award No. DMR 1734763.

WR acknowledges funding from the German Science Foundation (DFG), under the Emmy-Noether-Program (RH 146/1) and under the priority program “Fields Matter” SPP 1959 (HO1165/20).

### Abbreviations:

LLTO: Lithium Lanthanum Titanite $Li_{0.33}La_{0.57}TiO_3$; LCO: Lithium Cobalt Oxide

$LiCoO_2$; SPS: Spark Plasma Sintering; HRTEM: High-Resolution Transmission Electron Microscopy; SEM: Scanning Electron Microscopy; STEM: Scanning Transmission Electron Microscope; XRD: X-ray Diffraction; EIS: Electrochemical Impedance Spectroscopy; SE: solid electrolyte

## References

[1] J. Janek, W. G. Zeier, *Nat. Energy* **2016**, *1*, DOI 10.1038/nenergy.2016.141.

[2] A. Manthiram, X. Yu, S. Wang, *Nat. Rev. Mater.* **2017**, *2*, 1.

[3] J. Li, C. Ma, M. Chi, C. Liang, N. J. Dudney, *Adv. Energy Mater.* **2015**, *5*, 1.

[4] J. Wolfenstine, J. L. Allen, J. Sakamoto, D. J. Siegel, H. Choe, *Ionics (Kiel).* **2017**, 1.

[5] Z. Gao, H. Sun, L. Fu, F. Ye, Y. Zhang, W. Luo, Y. Huang, *Adv. Mater.* **2018**, *30*, 1.

[6] Y. Li, W. Zhou, X. Chen, X. Lü, Z. Cui, S. Xin, L. Xue, Q. Jia, J. B. Goodenough, *Proc. Natl. Acad. Sci.* **2016**, *113*, 13313.

[7] C. Sun, J. Liu, Y. Gong, D. P. Wilkinson, J. Zhang, *Nano Energy* **2017**, *33*, 363.

[8] H. Yamada, K. Suzuki, K. Nishio, K. Takemoto, G. Isomichi, I. Moriguchi, *Solid State Ionics* **2014**, *262*, 879.

[9] S. A. Pervez, M. A. Cambaz, V. Thangadurai, M. Fichtner, *ACS Appl. Mater. Interfaces* **2019**, DOI 10.1021/acsami.9b02675.

[10] Z. Wu, Z. Xie, A. Yoshida, Z. Wang, X. Hao, A. Abudula, G. Guan, *Renew. Sustain. Energy Rev.* **2019**, *109*, 367.

[11] Y. Seino, T. Ota, K. Takada, A. Hayashi, M. Tatsumisago, *Energy Environ. Sci.* **2014**, *7*, 627.

[12] N. Kamaya, K. Homma, Y. Yamakawa, M. Hirayama, R. Kanno, M. Yonemura, T. Kamiyama, Y. Kato, S. Hama, K. Kawamoto, A. Mitsui, *Nat. Mater.* **2011**, *10*, 682.

[13] Y. Harada, T. Ishigaki, H. Kawai, J. Kuwano, *Solid State Ionics* **1998**, *108*, 407.

[14] H. Aono, *J. Electrochem. Soc.* **1990**, DOI 10.1149/1.2086597.

[15] R. Murugan, V. Thangadurai, W. Weppner, *Angew. Chemie - Int. Ed.* **2007**, *46*, 7778.

[16] J. Haruyama, K. Sodeyama, L. Han, K. Takada, Y. Tateyama, *Chem. Mater.* **2014**, DOI 10.1021/cm5016959.

[17] K. H. Kim, Y. Iriyama, K. Yamamoto, S. Kumazaki, T. Asaka, K. Tanabe, C. A. J. Fisher, T. Hirayama, R. Murugan, Z. Ogumi, *J. Power Sources* **2011**, *196*, 764.

[18] R. Koerver, I. Aygün, T. Leichtweiß, C. Dietrich, W. Zhang, J. O. Binder, P.

Hartmann, W. G. Zeier, J. Janek, *Chem. Mater.* **2017**, *29*, 5574.

[19] K. Takada, *Acta Mater.* **2013**, *61*, 759.

[20] J. Haruyama, K. Sodeyama, L. Han, K. Takada, Y. Tateyama, *Chem. Mater.* **2014**, *26*, 4248.

[21] K. Nie, Y. Hong, J. Qiu, Q. Li, X. Yu, H. Li, L. Chen, *Front. Chem.* **2018**, *6*, 1.

[22] D. Santhanagopalan, D. Qian, T. McGilvray, Z. Wang, F. Wang, F. Camino, J. Graetz, N. Dudney, Y. S. Meng, *J. Phys. Chem. Lett.* **2014**, *5*, 298.

[23] A. Sakuda, A. Hayashi, M. Tatsumisago, *Chem. Mater.* **2010**, *22*, 949.

[24] K. H. Kim, Y. Iriyama, K. Yamamoto, S. Kumazaki, T. Asaka, K. Tanabe, C. A. J. Fisher, T. Hirayama, R. Murugan, Z. Ogumi, *J. Power Sources* **2011**, *196*, 764.

[25] W. D. Richards, L. J. Miara, Y. Wang, J. C. Kim, G. Ceder, *Chem. Mater.* **2016**, *28*, 266.

[26] K. Park, B. C. Yu, J. W. Jung, Y. Li, W. Zhou, H. Gao, S. Son, J. B. Goodenough, *Chem. Mater.* **2016**, *28*, 8051.

[27] S. Ohta, J. Seki, Y. Yagi, Y. Kihira, T. Tani, T. Asaoka, *J. Power Sources* **2014**, *265*, 40.

[28] T. Kato, T. Hamanaka, K. Yamamoto, T. Hirayama, F. Sagane, M. Motoyama, Y. Iriyama, *J. Power Sources* **2014**, *260*, 292.

[29] N. Ohta, K. Takada, L. Zhang, R. Ma, M. Osada, T. Sasaki, *Adv. Mater.* **2006**, *18*, 2226.

[30] T. Liu, Y. Ren, Y. Shen, S. X. Zhao, Y. Lin, C. W. Nan, *J. Power Sources* **2016**, *324*, 349.

[31] F. Han, J. Yue, C. Chen, N. Zhao, X. Fan, Z. Ma, T. Gao, F. Wang, X. Guo, C. Wang, *Joule* **2018**, *2*, 497.

[32] M. Gellert, E. Dashjav, D. Grüner, Q. Ma, F. Tietz, *Ionics (Kiel).* **2018**, *24*, 1001.

[33] L. Miara, A. Windmüller, C. L. Tsai, W. D. Richards, Q. Ma, S. Uhlenbruck, O. Guillon, G. Ceder, *ACS Appl. Mater. Interfaces* **2016**, *8*, 26842.

[34] O. Guillon, J. Gonzalez-Julian, B. Dargatz, T. Kessel, G. Schierning, J. Räthel, M. Herrmann, *Adv. Eng. Mater.* **2014**, *16*, 830.

[35] A. Aboulaich, R. Bouchet, G. Delaizir, V. Seznec, L. Tortet, M. Morcrette, P. Rozier, J. M. Tarascon, V. Viallet, M. Dollé, *Adv. Energy Mater.* **2011**, *1*, 179.

[36] Z. A. Munir, U. Anselmi-Tamburini, M. Ohyanagi, *J. Mater. Sci.* **2006**, *41*, 763.

[37] J. E. Garay, U. Anselmi-Tamburini, Z. A. Munir, *Acta Mater.* **2003**, *51*, 4487.

[38] Y. Ren, K. Chen, R. Chen, T. Liu, Y. Zhang, C. W. Nan, *J. Am. Ceram. Soc.* **2015**, *98*, 3603.

[39] S. Stramare, V. Thangadurai, W. Weppner, *Chem. Mater.* **2003**, *15*, 3974.

[40] W. J. Kwon, H. Kim, K. N. Jung, W. Cho, S. H. Kim, J. W. Lee, M. S. Park, *J.*

*Mater. Chem. A* **2017**, *5*, 6257.

[41] O. Bohnke, *Solid State Ionics* **2008**, *179*, 9.

[42] X. Yao, B. Huang, J. Yin, G. Peng, Z. Huang, C. Gao, D. Liu, X. Xu, *Chinese Phys. B* **2015**, *25*, 1.

[43] P. Xu, W. Rheinheimer, S. N. Shuvo, Z. Qi, O. Levit, H. Wang, Y. Ein-Eli, L. A. Stanciu, *ChemElectroChem* **2019**, *6*, 4576.

[44] Y. Takahashi, S. Tode, A. Kinoshita, H. Fujimoto, I. Nakane, S. Fujitani, *J. Electrochem. Soc.* **2008**, *155*, 537.

[45] K. Ozawa, *Solid State Ionics* **1994**, *69*, 212.

[46] Y. Ren, T. Liu, Y. Shen, Y. Lin, C. W. Nan, *J. Mater.* **2016**, *2*, 256.

[47] R. Aroshas, S. Kalabukhov, A. Stern, N. Frage, *Adv. Mater. Res.* **2015**, *1111*, 97.

[48] O. Levit, P. Xu, B. Shvartsev, G. Avioz Cohen, L. Stanciu, Y. Tsur, Y. Ein-Eli, *Energy Technol.* **2020**, *8*, 1.

[49] C. Ma, M. Chi, *Front. Energy Res.* **2016**, *4*, 1.

[50] Z. Wang, D. Santhanagopalan, W. Zhang, F. Wang, H. L. Xin, K. He, J. Li, N. Dudney, Y. S. Meng, *Nano Lett.* **2016**, *16*, 3760.

[51] S. Muto, K. Tatsumi, *Microscopy* **2017**, *66*, 39.

[52] P. R. Cantwell, M. Tang, S. J. Dillon, J. Luo, G. S. Rohrer, M. P. Harmer, *Acta Mater.* **2014**, *62*, 1.

[53] M. W. Barsoum, *Fundamentals Of Ceramics*, **2003**.

[54] S. P. Ong, A. Jain, G. Hautier, B. Kang, G. Ceder, *Electrochem. commun.* **2010**, *12*, 427.

[55] S. P. Ong, L. Wang, B. Kang, G. Ceder, *Chem. Mater.* **2008**, *20*, 1798.

[56] S. Plimpton, *J. Comput. Phys.* **1995**, *117*, 1.

[57] S. P. Coleman, D. E. Spearot, L. Capolungo, *Model. Simul. Mater. Sci. Eng.* **2013**, *21*, DOI 10.1088/0965-0393/21/5/055020.

[58] S. P. Coleman, M. M. Sichani, D. E. Spearot, *Jom* **2014**, *66*, 408.

[59] K. Chen, M. Huang, Y. Shen, Y. Lin, C. W. Nan, *Solid State Ionics* **2013**, *235*, 8.

[60] Y. Inaguma, C. Liquan, M. Itoh, T. Nakamura, T. Uchida, H. Ikuta, M. Wakihara, *Solid State Commun.* **1993**, *86*, 689.

[61] T. Hang, D. Mukoyama, H. Nara, N. Takami, T. Momma, T. Osaka, *J. Power Sources* **2013**, *222*, 442.

[62] R. A. Huggins, *Advanced Batteries: Materials Science Aspects*, **2009**.

[63] S. Wenzel, T. Leichtweiss, D. Krüger, J. Sann, J. Janek, *Solid State Ionics* **2015**, *278*, 98.

[64] Y. Liu, Q. Sun, D. Wang, K. Adair, J. Liang, X. Sun, *J. Power Sources* **2018**, *393*, 193.